Supplementary Information

Coherent-Interface-Assembled Ag_2O-Anchored Nanofibrillated Cellulose Porous Aerogels for Radioactive Iodine Capture

Yun Lu,[a] Hongwei Liu,[b] Runan Gao,[c] Shaoliang Xiao,[c] Ming Zhang,[c] Yafang Yin,[a] Siqun Wang,[a,d] Jian Li,[c]* and Dongjiang Yang[e,f]*

a. Research Institute of Wood Industry, Chinese Academy of Forestry, Beijing 100091, China.

b. Australian Center for Microscopy & Microanalysis (ACMM), The University of Sydney, Sydney, NSW 2006, Australia.

c. Material Science and Engineering College; Key Laboratory of Bio-based Material Science and Technology, Ministry of Education, Northeast Forestry University, Harbin 150040, China.

d. Center for Renewable Carbon, University of Tennessee, Knoxville, TN, 37996, US

e. Queensland Micro- and Nanotechnology Centre (QMNC), Griffith University, Nathan, Brisbane, Queensland 4111, Australia.

f. College of Chemistry, Chemical and Environmental Engineering; Laboratory of Fiber Materials and Modern Textile, the Growing Base for State Key Laboratory, Qingdao University, Qingdao 266071, China.

Corresponding Authors * E-mail: jianli@nefu.edu.cn; d.yang@qdu.edu.cn

Experimental Details

Raw Materials and Chemicals： Silver nitrate ($AgNO_3$, A.R.), Sodium iodide (NaI, 99%), iodine (A.R.), sodium chlorite ($NaClO_2$, A.R.), potassium hydroxide (KOH, A.R.), sodium hydroxide (NaOH, A.R.) and *tert*-butanol (*t*-BuOH, A.R.) were purchased from Aladin Chemical Co. Benzene, ethanol, acetic acid, ammonia ($NH_3 \cdot H_2O$, 28%), hydrochloric acid were purchased from Shanghai Chemical Industrial Co. Ltd. and used as received without further purification. Mature culms of Moso bamboo (*Phyllostachys Sieb.*) were collected from Jiangsu Province, China. All samples sieved under 60 mesh were air-dried and stored at room temperature.

Synthesis of Nanofibrillated Cellulose (NFC)： The bamboo NFC was prepared by chemical pretreatment and high-intensity ultrasonication. Firstly, dried bamboo powders were purified to prepare the predecessor of cellulose nanofibers. Immersed about 5 g bamboo powers in a Soxhlet apparatus with a 2:1 (V:V) mixture of benzene and ethanol at 90 °C for 6 h under reflux to remove organic soluble extractives followed by rinsing with water. And then treated with an acidified sodium chlorite solution (1.5 wt% $NaClO_2$, buffered with acetic acid to pH 4.0) at 80 °C for an hour, and this process was repeated for 5 times. Next, the samples were then treated with 5 wt% potassium hydroxide at 90 °C for 2 h to remove lignin, hemicelluloses, and residual starch. These steps of acidified $NaClO_2$ and alkali treatments were repeated twice, followed by filtration and washing with distilled water. Highly purified cellulose fibers were prepared by further treating the samples with a 1 wt% hydrochloric acid solution at 80 °C for 2 h and thoroughly washing them with distilled water to remove excess salt. Since drying process of cellulose fibers generates strong hydrogen bonding between fibers, cellulose must be kept wet after purification for the next nanofibrillation.

For the promotion of nanofibrillation, the purified wet cellulose was dispersed in water, about 400 mL water slurry containing 0.1 wt% sample. And sonications were performed at 25 kHz

with a common ultrasonic generator (JY99-IID, Ningbo Scientz Biotechnology Co., Ltd., China) with a 1 cm^2 titanium horn. The subsequent ultrasonication experiments were performed under a 50% duty cycle (i.e., a repeating cycle of 0.5 second ultrasound on, 0.5 second ultrasound off) in order to reduce temperature variation, and conducted for optical time length with an output power of 1 000 W to isolate the fibers. Ultrasonic treatment was carried out in an ice/water bath, and ice was maintained throughout the entire ultrasonication. In order to remove the fibril aggregates and contaminants from the sonication probe, the dispersion was centrifuged at 5000 rpm, and only the supernatant was used in the experiments. The water suspension containing NFC will be obtained after 5 min centrifugation.

Preparation of NFC aerogel: The NFC/water suspension was subjected to dialysis tubing cellulose membrane (flat width 76 mm, Sigma-Aldrich), which was subjected to solvent-exchange with *t*-BuOH. After solvent changing, the NFC aerogels with a cellulose faction of 0.5 vol% containing *t*-BuOH were poured into molds, and then placed in a refrigerator at -55 °C and freeze-dried 4 h at 25 μPa using a Scientz-10N freeze-dryer (BT6K-ES, Virtis). The NFC aerogels with open porous structure were obtained after all these drying processes.

Fabrication Ag_2O NPs in NFC aerogel: Dried aerogel pieces (10 mg) were immersed in 0.04 dm^3 of freshly prepared ammoniated silver solution with a molar ratio of $[Ag]/[NH_3]=1:2$. Then swell 5 min and ultrasonic for another 5 min to ensure a homogeneous distribution of the cellulose networks. Three different solutions with total concentrations of the $Ag(NH_3)_2OH$ ($[Ag]/[NH_3]=1:2$) of 5×10^{-2} mol dm^{-3} (sample Ag_2O@NFC-050), 1×10^{-2} mol dm^{-3} (sample Ag_2O@NFC-010), and 5×10^{-3} mol dm^{-3} (sample Ag_2O@NFC-005) were used. The systems were freeze-dried to get white composite gels. The cellulose network was subsequently transferred into 0.04 dm^3 of dilute NaOH solution (pH=10) at room temperature. The color of the samples slowly changed from white to brownish-black as nanoparticles formed. To

complete the reaction, the system was kept without disturbance for an addition 12 h at room temperature. All these reactions were performed in air (Figure 1).

The particle-modified NFC network was then washed thoroughly. The obtained particle-functionalized networks were immersed in liquid nitrogen and freeze-dried to generate the elastic and porous monolithic aerogel nanocomposites, with well-defined Ag_2O nanoparticles assembled along the NFC scaffold. The final product was named Ag_2O@NFC, according to the starting NFC aerogel. After a deposition of Ag_2O nanocrystals, the color of the aerogels turned to brownish-grey. With the subsequent adsorptions of iodine and I^- anions, the nanocomposites color then changed to light yellow.

Capture of Iodine: A 500 mg portion of I_2 was transferred in a two neck round-bottom flask. On the top of the flask, a fritted glassware was connected where a piece (10 mg) of Ag_2O@NFC was placed. Iodine vapors were produced after heating the flask at 75 °C, and they were driven upward with the nitrogen flow connected from the side neck of the flask.

I^- anion adsorption of Ag_2O@NFC aerogels: In the present study, because of higher radiation dose of $^{131}I^-$, we used stable I^- anions to monitor the behaviour of $^{131}I^-$ isotope. The two isotopes, however, have the same chemical reaction properties. 10 mg adsorbents (Ag_2O@NFC-005, Ag_2O@NFC-010, and Ag_2O@NFC-050) were used as sorption beds to catch I^- ions from 50 ml required concentration (50 ppm, 125 ppm, 250 ppm, 350 ppm, 500 ppm, 750 ppm, and 1000 ppm) of NaI (Sigma-Alderich, 99%) aqueous solutions. The flow rate was kept at 5.0 mL min^{-1}. The filtered solutions were collected to determine the concentration of I^-. The supernatants were introduced into a quartz cuvette, and the concentrations of I^- were measured from 200 to 400 nm using a UV-vis spectrophotometer (UV-1800, Shinadzu Corp., Japan). The spectrum of a cuvette filled with deionized water was used as a reference.

Characterization: The bulk density of the NFC and Ag_2O@NFC aerogels was determined from the dimensions and weights of the samples.

The porosity of the products was calculated using the bulk density of the aerogels (d_a) and the density of the crystalline native cellulose (d_c=1.6 g cm^{-3}) using the following formula:

$$\text{Porosity } \% = (1 - d_a / d_c) \times 100\%$$

The macroscopic appearances of the products were observed through visual examination. The EDS spectra and scanning electron microscopes (SEM) images were recorded on a FE-SEM (Sirion 200, FEI) and FEI Quanta 200 SEM-EDS (EDS/EDX Genesis, EDAX Inc.) where the SEM was equipped with elemental analysis capabilities. The SEM images were taken by using an auto fine coater (JFC-1600; JEOL Ltd.) to coating the samples with gold to improve the conductivity. Drops of dilute aerogel network suspensions (acetone) were deposited onto glow-discharged carbon-coated TEM grids. The excess liquid was absorbed by a piece of filter paper. After the specimen has been completely dried, transmission electron microscopy (TEM) was observed under an FEI Tecnai G2 electron microscope operated at 80 kV. High-resolution transmission electron microscopy (HRTEM) was performed at 90 K using a JEOL-2011 at 200 KV.

In order to reveal Ag_2O decoration nature of Ag_2O@cellulose nanocomposite, an electron tomography characterization was carried out on JEM-2100 and JEM tomography recorder. A single-tilt tomography holder was applied. The tilting angle range falls in -65° to 65°. The tilt step is 1°. The total tilted images are 130 frames. All of them were collected under well-aligned microscope environment. High diffraction contrast was set by inserting small–diameter objective aperture.

The thermogravimetric analysis (TGA) was performed in a thermogravimetric analyzer (Pyris 6, PerkinElmer, USA) by heating each sample (ca. 10 mg) from 25 °C to 800 °C with a heating rate of 10 °C/min in a nitrogen environment.

The X-ray diffraction (XRD) patterns of the NFC, Ag_2O@NFC and the corresponding aerogels after reactions were measured with an XRD (D/max 2200, Rigaku) using Ni-filtered Cu Kα radiation (λ=1.5406 Å) at 40 kV and 30 mA. Scattered radiation was detected in the range of 2θ=10°–80° at a scan rate of 4°/min. The precision and accuracy of the diffraction peak positions resolved from the diffraction spectra of raw materials and products by means of PeakFit® (Sea-Solve Software Inc., Richmond, CA) to evaluate the suitability of such a method to disclose aspects of the cellulose's crystalline structure not readily apparent in its diffraction spectrum.[1] The crystallinity index (*Cr*I) is obtained as the ratio of the area arising from the crystalline phase to the total area.[2]

The FTIR spectra were recorded on a Fourier transform infrared instrument (Magna 560, Nicolet, Thermo Electron Corp) in the range of 400 cm^{-1}-4000 cm^{-1} with a resolution of 4 cm^{-1}. All the samples were ground into powder by a fiber microtome and then blended with KBr before pressing the mixture into ultra-thin pellets.

X-ray photoelectron spectroscopy (XPS) (SSX-100 ESCA spectrometer) and X-ray Auger Electron Spectroscopy (XAES) were used to study the composition of the composite samples. The XPS equipped with rotating anode of special UHV design. The photoelectrons were excited using monochromatized AlKα X-rays (hν=1486.6 eV). The samples were spread on gold plates, which were mounted on a sample probe by means of tantalum clips. Detailed spectral scans were taken over the Ag 3d, Ag MNN, and I 3d spectral regions. The instrument was calibrated so that the difference between the Au $4f_{7/2}$ photoelectron peak and the Fermi level was 84.0 eV. The spectrometer was operated in the fixed analyser transmission mode. The background pressure of the residual gases during spectral accumulation was typically of the order of ~10^{-7} Pa. The C 1s binding energy (285 eV) of adventitious hydrocarbon was used as an internal standard in calibration to compensate for static surface charging of the sample. The XPS measurements were carried out on the samples in the as-received state. The

peak positions and areas were determined by fitting the unsmoothed experimental data after subtraction of the Shirley background.[3] Quantification of the element surface concentration ratios was accomplished by correcting the integral intensities of the photoemission peaks for their cross-sections[4] and accounting for the dependence of the analyser transmission[5] and electron mean free paths on kinetic energy of electrons.[6] Core level binding energies were determined with an accuracy of ±0.2 eV. The spectra de-convolution into a minimum number of the components was done by application of the Voigt-type line shapes (70:30 Gian/Lorentzian product).

The Brunauer-Emmet-Teller (BET) surface area (S_{BET}) and pore properties of the samples were determined from N_2 adsorption-desorption experiments at −196 °C using an accelerated surface area and porosimetry system (3H-2000PS2 unit, Beishide Instrument S&T Co., Ltd). All the samples were outgassed at 120 °C for 10 h to remove any moisture or adsorbed contaminants prior to the surface area measurements. The pore-size distributions were estimated by the Barrett-Joyner-Halenda (BJH) method.[7,8]

Ultrasonication treatments and NFC diameter distributions

In the ultrasonication process, the bamboo cellulose component was firstly extracted from the bamboo powder after chemical purification. After chemical pretreatment, highly purified bamboo cellulose fibres were soaked in distilled water at approximately 0.1% (w/w) solid content. The subsequent ultrasonication was conducted for 10 min, 20min, and 30 min at an output power of 1 000 W, resulting in a cellulose nanofibrils suspension. As shown in Scheme 1, the purified bamboo cellulose suspension with a concentration of 0.1 wt% was passed through an ultrasonic processor for nanofibrillation. This strategy is based on an ultrasonication mechanism: ultra-sonication causes the natural fibres to disassemble into nanofibres in water via cavitation, formation, growth, and implosive collapse of bubbles in the solution.[9] For instance, small gas bubbles (cavities) will be generated in a cellulose aqueous suspension when the suspension is treated by ultrasound. These small gas bubbles are able to absorb energy from the sound waves and grow rapidly under high ultrasound intensities. However, the cavity implodes when the cavity has overgrown, and the surrounding liquid rushes in. The implosion of the cavity creates an unusual environment and introduces high-pressure and shock waves within a short time. This violent collapse causes direct particle-shock wave interactions and is the primary pathway to split cellulose fibres along the axial direction. Thus, the sonification impact breaks the relatively weak bamboo cellulose interfibrillar hydrogen bonding and the Van der Waals force, gradually disintegrating the micro-scale bamboo cellulose fibres into nanofibres.

Figure S1a shows the microstructure of the bamboo cellulose fibres after 10 min ultrasonic process. Figure S1b and S1c show SEM images of the sample after 20 and 30 min of ultrasonic treatment, respectively. The bamboo cellulose microfibrils were disintegrated to the nanoscale in the ultrasonication process, and diameter of the separated bamboo cellulose nanofibrils decreased with increasing ultrasonic treatment time. The diameter distributions of

the cellulose fibres treated by the ultrasonication process were calculated by the Nano Measure software and are illustrated in Figure S1d-f. Firstly, the dominant fibres diameter decreases with the increase of ultrasonication treatment time. For instance, the dominant fibres diameter after 10 min is 244.4 nm and the value decreases to 67.2 and 51.9 nm for 20 min and 30 min, respectively. Secondly, the diameter distribution of the ultrasonication treated samples becomes narrower with the increasing ultrasonication time. Obviously, ultrasonication treatments not only disintegrated cellulose fibres, but also efficiently modified the diameter distribution of the fibres by facilely changing the ultrasonic treatment times. The results revealed that plentiful slender cellulose nanofibrils were generated by 1000 w pulsed ultrasonic treatment for 30 min, which is the key to form nanofibrils under 80 nm in diameter. With high aspect ratio, the homogeneous nanofibrils is ideal scaffold materials for supporting functional metal oxide nanoparticles, and also have appealing mechanical performance.

Functionality of silver oxide

Silver (I) oxide (Ag_2O) has been widely used in many industry field as cleaning agents, colorants, and electrode materials. In recent years, Ag_2O has attracted researchers' increasing interests because of its high activity and selectivity to react with iodine to form insoluble silver iodide (AgI).[10] Captures of I_2 and I^- ions are of special interests because radioactive ^{131}I and ^{129}I are the byproducts of uranium fission and can be easily released in air and dissolved in water during an accident at a nuclear reactor. Additionally, radioactive ^{125}I is used in the treatment of thyroid cancer and as a result, the radioactive wastewater is discharged by a large number of medical research institutions.[11] However, using Ag_2O directly for the removal of I^- anions is impractical as the capacity and dynamics of the removal depends on the specific surface area of the Ag_2O particles. If the specific surface area is small (large Ag_2O particles), the removal ability is poor. When very fine Ag_2O particles with a large specific surface area are used, the removal ability is improved but the separation of the used Ag_2O particles from water will be extremely difficult and costly. Many pioneer works[12] recently produced 1D Ag_2O composited titanate-based nano-adsorbents and also pointed out the solution of the upper problem is to anchor fine Ag_2O nanocrystals firmly on to a support with a large specific surface area that allows them to disperse sufficiently without aggregates. Moreover, the support should be maintained certain morphology that it can be readily separated form liquid after use. Many polymer-nanoparticle composites showed extensive attractive for multifunctional characteristics, and their mechanical, optical and catalytic properties. The challenge is access an inexpensive, green and scalable process. Nowadays, there is a trend to produce nanostructured materials from biomass materials, as they are very cheap, easy to obtain, and nontoxic to humans, *etc*. The qualified nanofibrillated cellulose (NFC), native cellulose I nanofibers disintegrated easily from plant cells, is an attractive form of scaffold. Thus, we developed NFC assembled aerogels as templates for the growth of 10~20 nm

diameter Ag_2O nanoparticles to form Ag_2O@NFC aerogel. The Ag_2O@NFC also has high surface area, low bulk density, and can contain Ag_2O as high as 92% of its mass without any agglomeration, which is able to capture significant amount iodine vapor forming mainly AgI but also in the molecular form. These Ag_2O nanoparticles act as efficient captures as they are exposed on the surface of every single NFC nanofiber and thus readily accessible to I^- ions from contaminated water even in a fast flux.

Ag_2O nanoparticles size distributions

After deposition of Ag_2O NPs (10~20 nm), the smooth surface of 80 nm diameter pure NFC turns to very rough (Figure S3). When the concentration of $Ag(NH_3)_2OH$ raises from 5×10^{-3} M to 1×10^{-2} M, the increasing inorganic contents covert composite scaffolds from curly soft to straight hard (Figure S4). As shown in Figure S5, the size of Ag_2O NPs increases from 10 to 16 and 21 nm, And the color of final Ag_2O modified NFC products changes from light to dark (insets of Figure S5). The inorganic Ag_2O species can be controlled to ~54 wt% (Ag_2O@NFC-005), ~72 wt% (Ag_2O@NFC-010) and ~92 wt% (Ag_2O@NFC-050) in final composites, respectively. As depicted in X-ray diffraction (XRD) patterns (Figure S5d), a typical native cellulose I structure is observed for the NFC aerogel, where cellulose chains packed in a "parallel up" fashion in the unit cell (Figure S6). The diffraction peaks at 14.8, 16.5, 22.5, and 34.8° are ascribed to (101), $(10\bar{1})$, (002) and (040) planes, respectively. In addition, the deposited Ag_2O NPs display a typical cubic structure (JCPDS no. 41-1104). The crystallite sizes determined from Scherrer equation range from 9 to 14 and 20 nm for Ag_2O@NFC-005 to Ag_2O@NFC-010 and Ag_2O@NFC-050. The nanoparticle structures were tuned by changing concentrations of starting $AgNO_3$ and ammonia (with a fixed molar ratio of 1:2) from 0.005 mol dm^{-3} (Ag_2O@NFC-005) to 0.01 mol dm^{-3} (Ag_2O@NFC-010) and 0.05 mol dm^{-3} (Ag_2O@NFC-050) while keeping the dry NFC aerogel (0.25 mg cm^{-3}) volume fraction constant (see Table S1 for more details). With the different concentration of the Tollens reagents (the resulting $Ag(NH_3)_2^+$ solution in Eq. 1), the color of final Ag_2O modified NFC products changed from light to dark, and the sizes of Ag_2O particles are also determined by the concentration of the Tollens reagents.

Mechanism of Interactions between Ag_2O nanoparticles and NFC

FT-IR spectrum (Figure S7) of Ag_2O@NFC demonstrated that Ag_2O nanoparticles interacted to NFC by non-covalent bonds. Meanwhile, the appearance of cellulose I_β characteristic bands verified the presence of NFC in composite materials. It is worth noting that the wavenumber of the stretching band of the hydroxyl groups of NFC decreased from 3468 cm^{-1} to 3397 cm^{-1}, and the stretching vibration of C-O bond of NFC located at 1060 cm^{-1} and 1037 cm^{-1} has a serious distortion in composites. These phenomena revealed the formation of strong hydrogen bonds between Ag_2O and NFC. For the Ag_2O, The 2975 cm^{-1}, 2924 cm^{-1}, and 2854 cm^{-1} vibrational bands should be assigned to O-H bending vibration and C-O absorption. Generally, the absorption bands are due to the presence of bending and stretching vibrations of carbon dioxide. The observed broad peak around 3397 cm^{-1} and the peak at 1456 cm^{-1} belonged to the O-H stretching vibration, while the peak at 1385 cm^{-1} belonged to the H-O-H bending vibration of the adsorbed water molecules on the surface.[13] Usually semiconductor nanostructure materials absorb carbon dioxide and water from the environment, due to their high surface-to-volume ratio of mesoporous nature.[14,15]

Electron tomography (ET), is a method for generating 3D images, on the basis of multiple 2D projection images of a 3D object, obtained over a wide range of viewing directions (Figure S8). The theory of electron tomography is shown in Figure S8 a-c. At the exact focus plane of objective lens, the sample is tilted systematically around X-axis to obtain a serial of tilted image. The reconstruction of the tomography data is time-consuming and the quality of reconstructed 3D image is determined by microscope environment, alignment condition, and sample preparing condition and diffraction contrast effect. An animated GIF image is provided as 3D movie (Movie S1) which clearly shows the evidence that nanosized Ag_2O crystals are decorating on surface area but not embedded into the inner part of the cellulose nanofibres. The 3D tomography image also indicated a well-developed crystallinity of Ag_2O

nanocrystals while cellulose nanofibres were easy to lose its crystalline state. Finally, the binding between Ag_2O and cellulose naofibre was very tight. This could be verified by 3D tomography image, in which Ag_2O particles were highly enclosing on nanofibres (Figure S8d).

TEM technique was also used to reveal possible crystal interfaces or interphase boundaries between Ag_2O NPs and NFC. The diffraction pattern (EDP) of a single Ag_2O/cellulose nanofibre (Figure 1a) was displayed in Figure 1b. Obviously, multiple diffraction rings could be indexed with the lattice parameters of both cellulose and Ag_2O. The former has a monoclinic structure with lattice parameters of a = 0.7784 nm, b = 0.8021 nm, c = 1.038 nm, gamma = 96.55°. The latter is face-centred cubic (FCC) structure with lattice parameters of a = 0.475 nm. The highest intensity rings of each phase are clear and sharp and belong to (011) of Ag_2O and (200) of cellulose. The FCC-structured Ag_2O NP in Figure 1a had a typical five-fold twinning feature, which is a common twinning feature for cubic structural phase.

The fast Fourier transformation (FFT) images of the selected areas in Figure 1a were displayed in Figure S9a-c. Figure S9d-f represented the indexed results from the FFT images. Clearly, cellulose grown along its lone axis parallel to [001] direction while the wide surface was ($\bar{1}$10) of the Ag_2O NPs. Figure 1c showed [110] diffraction pattern of Ag_2O while Figure 1d had a complicated pattern as it includes moiré fringe with three times of planar *d*-spacing of (110). It was due to overlapping of two crystals of Ag_2O. Figure 3e indicated (002)s//(110)c and (001)c//(110)s. Here ′s′ and ′c′ denoted ′Ag_2O′ and ′Cellulose′, respectively. Figure 1f showed the scheme of interface structure (001)c//(110)s. Please note that the planar *d*-spacing of (001)c (1.038 nm)was exactly six time of that of (110)s (6 time of the interplanar space is 1.02 nm). Their similar interplanar distances meaned there were a good coincidence of atomic planar matching at this interface (coherent interfaces). And Ag_2O nanocrystals were firmly anchored to the NFC nanostructure by such coherent interfaces. It could deduce that

Ag_2O had a high-density distribution on cellulose surface as shown in a BF image of Figure 1g.

I^- anion adsorption of Ag_2O@NFC aerogels

The *in situ* wet chemical method allowed the entire surface of open pore NFC aerogel decorated with Ag_2O nanocrystals. The fabrication of a facile template approach to metallic oxide nanocomposites of hydrogels/aerogels consisting of NFC is a simple template-directed wet chemical process. Specifically, the composite aerogels, which combined the advantages of flexibility and excellent adsorption capacity, were able to use directly as compressible super-absorbents. In this work, the Ag_2O@NFC aerogels capture and immobilize I^- ions from water.

After I^- anion adsorption, over 90 % of I^- ions (lower than 500 ppm) were removed by Ag_2O@NFC-005. Ag_2O@NFC-050 showed 100% adsorptive capacity of I^- ions. The capacities of the Ag_2O@NFC sorbents for I^- ion sorption can be derived from the isotherms illustrated in Figure 3b. The approximate uptake capacity of the Ag_2O@NFC-050 is 5.2 mmol of I^- anions per gram of sorbent, while the capacity for the Ag_2O@NFC-010 was slightly lower at 4.7 mmol g^{-1}, and the capacity for the Ag_2O@NFC-005 was the lowest at 3.0 mmol g^{-1} These uptake values are considerably higher than the values of less than 1.0 mmol g^{-1} previously reported for conventional metallic compound sorbents.[16]

The fast kinetics can be attribute as follows: (1) the interpenetrating, open-pore network characteristic of aerogel scaffold permits rapid transport of liquid-phase reactants and objects into, throughout, and out of the structure.[17,18] (2) The Ag_2O nanocrystals firmly anchored onto the NFC surface, which made the capture of I^- much more efficient. (3) The small Ag_2O nanocrystals without aggregate together had faster chemical reactivity to precipitate I^- anions than the bulk Ag_2O, which makes the higher adsorption capacity towards ionic pollutants.

Figure S13 is the schematic illustration of the Ag_2O nanocrystal formation on the (001) plane of cellulose nanofibers within the NFC aerogel and the subsequent deposition of I^- ions. NFC was consisted of monoclinic cellulose I_β, and the exposed plane is mainly (001). When

$Ag(NH_3)_2^+$ ions diffused on the surface of the NFC in a basic environment, silver hydrate $Ag(OH)_n(H_2O)_m$ intermediates will form and deposit on the surface. The dehydration process of silver hydrate intermediates will take place on the outermost surface (001) planes of cellulose I_β. Therefore, the surface plane (001) was seriously deformed, and resulted the dramatic loss of diffraction intensity of this plane after Ag_2O nanocrystals precipitation. After the entrapment of iodine ions, AgI nanocrystals formed onto the NFC surface. And the joint interface between the AgI nanocrystals and the NFC surface might be composed of the silver atoms and the hydroxyl groups of cellulose molecules. Hence, the significant deformation was still retained after deposition of I^- ions since the precipitation of Ag_2O nanocrystals, as indicated by the XRD patterns (Figure S12). That makes the composite gels have further application potential as novel sorbents for I^- ions solution cleanup.

Figures

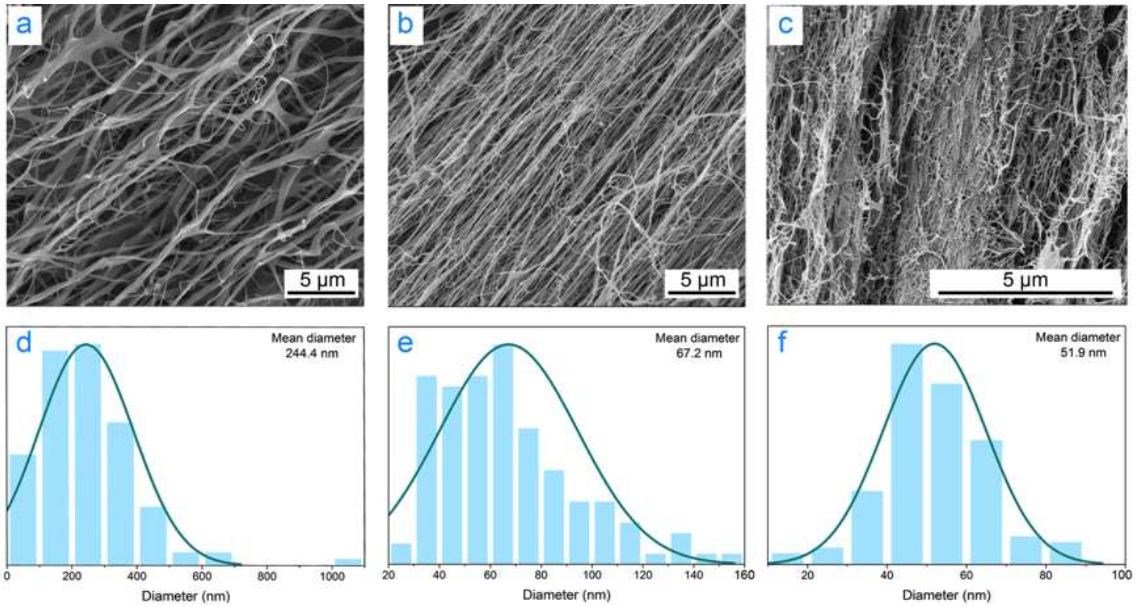

Figure S1. Morphology and diameter distributions of bamboo cellulose with different ultrasonication time. SEM micrographs of chemical purified bamboo cellulose (a) after 10 min, (b) after 20 min and (c) after 30 min ultrasonication (1 000 W, 25 kHz). (d), (e), and (f) are the corresponding diameter distributions of the fibres of (a), (b) and (c). Histograms of the fibres diameter based on a statistical method, which suggests an average value of 244.4 nm, 67.2 nm and 51.9 nm, respectively. The lines are normal distribution curves.

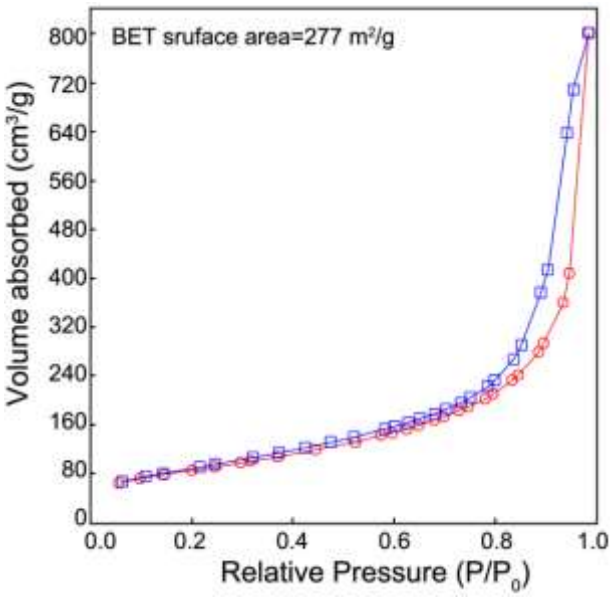

Figure S2. Nitrogen adsorption (open circles) and desorption isotherm (open squares) measured at 77K for the NFC aerogel by *t*-BuOH freeze-drying.

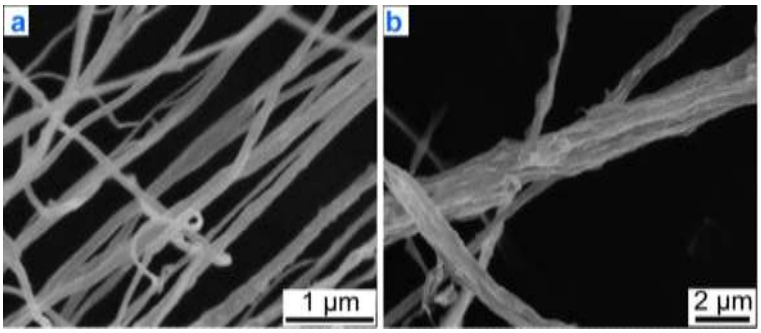

Figure S3. Scanning electron micrographs of the networks of the NFC aerogel and Ag_2O@NFC aerogel. (a) The pure NFC fibrils dispersed well with clear surface, (b) Ag_2O decorated Ag_2O@NFC networks aggregated with rough surface.

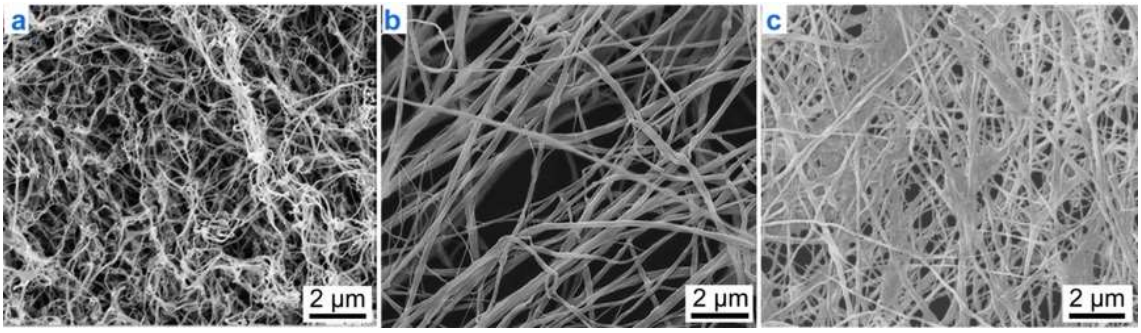

Figure S4. Scanning electron micrographs of Ag_2O@NFC aerogels with different Ag_2O contents. (a) Curly Ag_2O@NFC-005 networks, (b) straight Ag_2O@NFC-010 networks with part aggregation, and (c) Ag_2O@NFC-050 networks with much more aggregation.

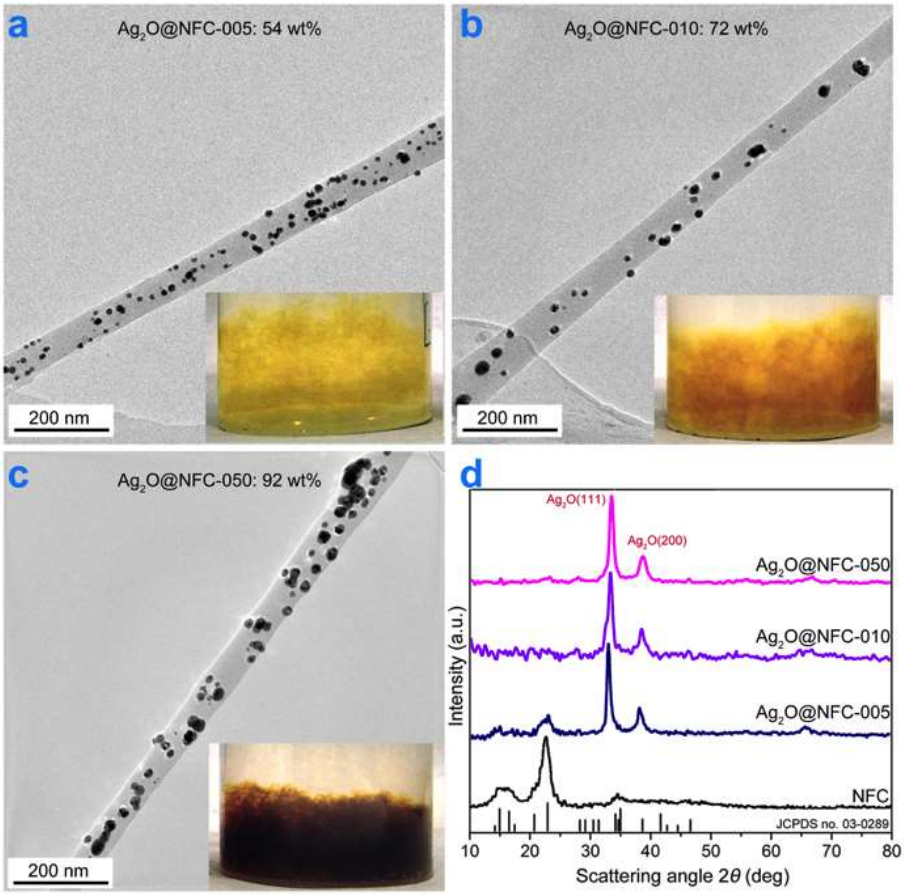

Figure S5. Ag_2O@NFC aerogels at different loadings of Ag_2O nanocrystals. TEM images of abundant Ag_2O crystals dispersed on NFC for a) sample Ag_2O@NFC-005 (54 wt% of crystals), b) Ag_2O@NFC-010 (72 wt% of crystals) and c) Ag_2O@NFC-050 (92 wt% of crystals). d) X-ray diffraction (XRD) patterns for Ag_2O@NFC-005, Ag_2O@NFC-010, and Ag_2O@NFC-050 with different Ag_2O compositions. Unmodified NFC is shown as a reference. The position of the Ag_2O (red character, JCPDS no. 41-1104) and the cellulose (black vertical lines, JCPDS no. 03-0289) peaks are marked.

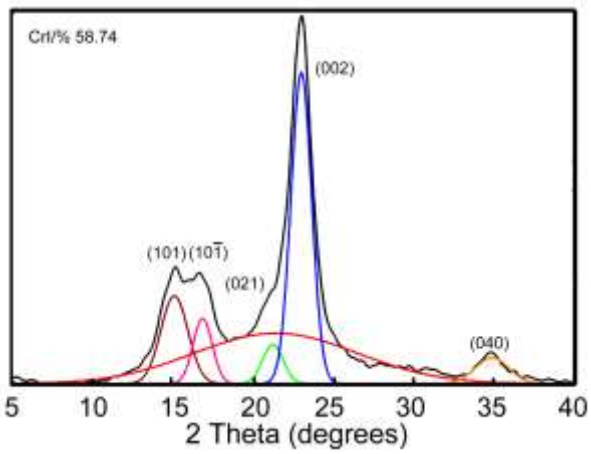

Figure S6. The XRD pattern of the pure NFC aerogel. The most obvious diffraction peaks are at 14.8°, 16.5°, 22.5°, corresponding to the plane $(101)_c$, $(10\bar{1})_c$, and $(002)_c$ of cellulose.

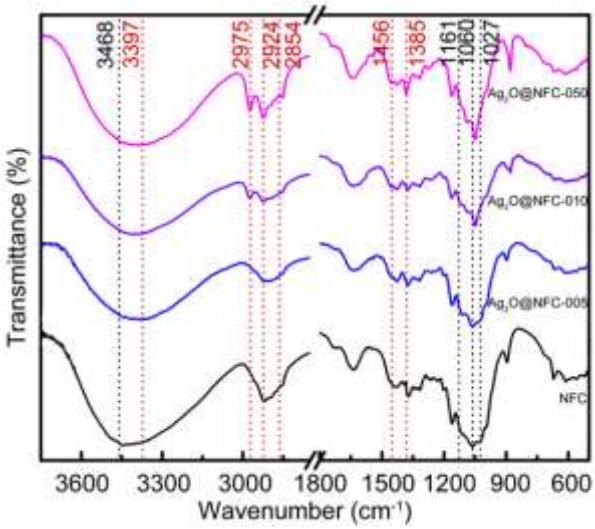

Figure S7. FT-IR spectrum of pure NFC aerogels and Ag_2O@NFC aerogels (Ag_2O@NFC-005, Ag_2O@NFC-010, and Ag_2O@NFC-050) after Ag_2O nanoparticles deposition.

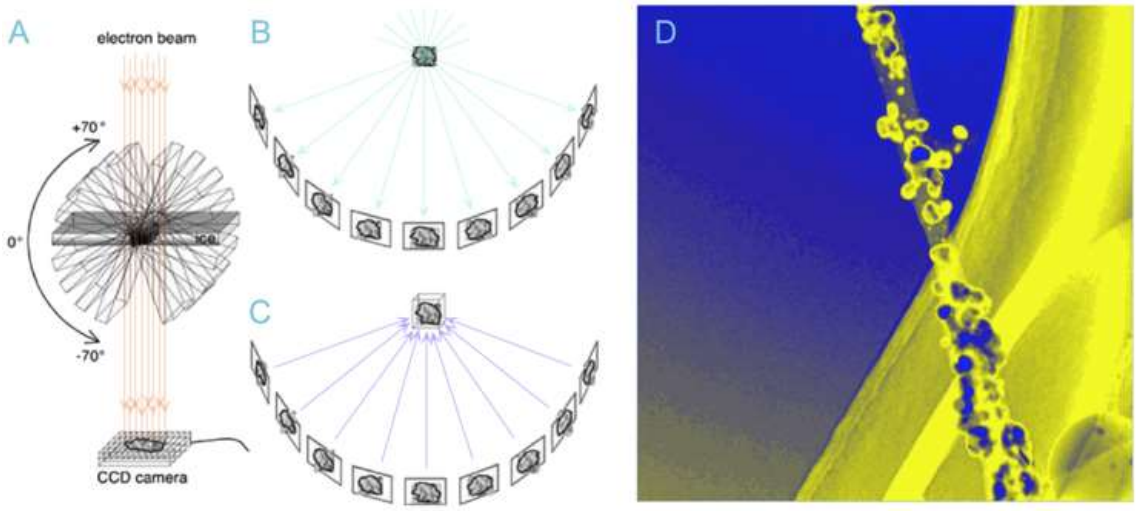

Figure S8. Scheme of electron tomography (ET) and the 3D representation of the Ag_2O@NFC-100 obtained by electron tomography. (a) and (b) A specimen contained in an EM sample holder, can be imaged from several orientations by tilting the holder in the microscope. (c) Process of computed back-projection, in which each tilted view is used with appropriate weighting to contribute to a reconstruction of the original structure to generate the sought-after 3D image. (d) The 3D electron tomography of Ag_2O@NFC-100 nanostructures.

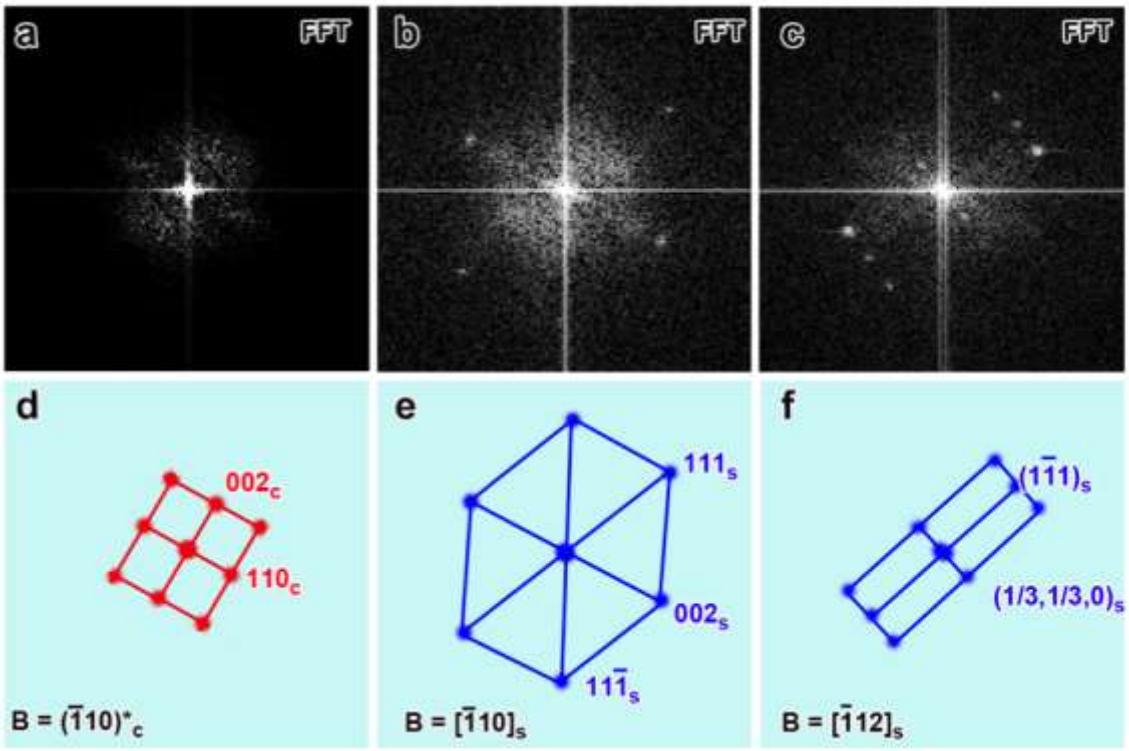

Figure S9. The Fast Fourier Transformation (FFT) images of the transmission electron microscopic (TEM) investigation of Ag_2O@NFC and the corresponding indexed results of the FFT images. (a), (b), and (c) The Fast Fourier Transformation (FFT) images corresponding to the selected areas marked in Fig.1 A with label c, d, e, respectively. (d), (e), and (f) The indexed results of the FFT images in Panels a, b and c, respectively.

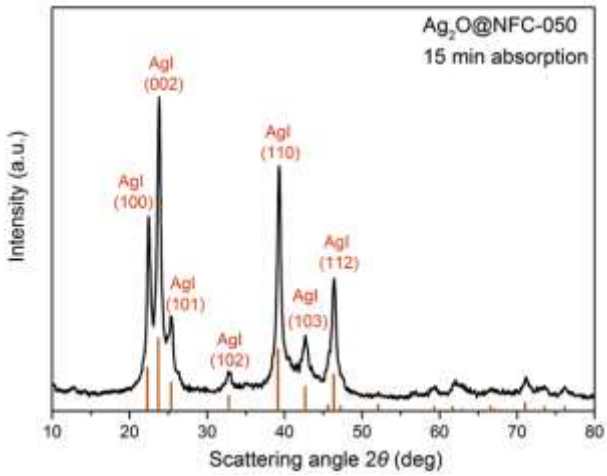

Figure S10. The XRD pattern of the Ag_2O@NFC-050 aerogel captured and stabilized iodine vapor for 15 min to form AgI@NFC. The vertical lines at bottom mark the position of hexagonal β-AgI (JCPDS no. 09-0374) peaks.

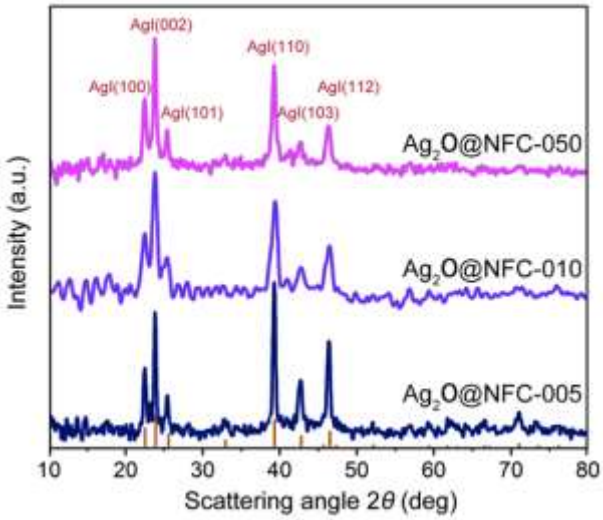

Figure S11. XRD patterns for the AgI@NFC-005, AgI@NFC-010 and AgI@NFC-050 after adsorption of I^- ions. The vertical lines at bottom mark the position of hexagonal β-AgI (JCPDS no. 09-0374) peaks.

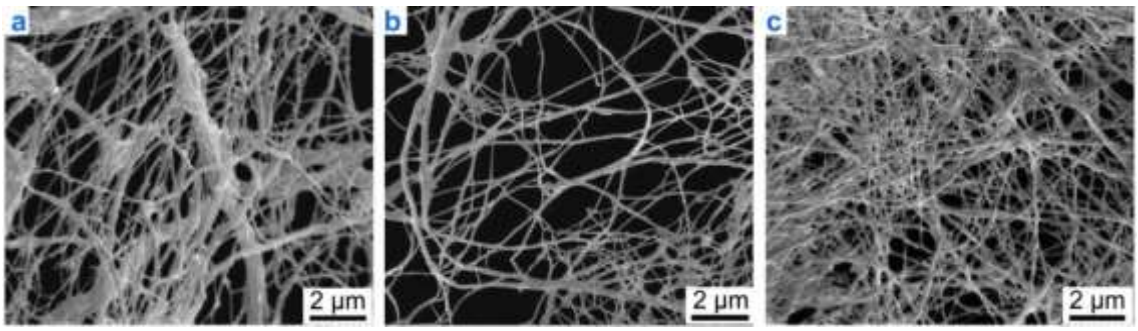

Figure S12. Scanning electron micrographs of AgI@NFC aerogels. (a) AgI@NFC-005 networks, (b) AgI@NFC-010 networks, and (c) AgI@NFC-050 networks.

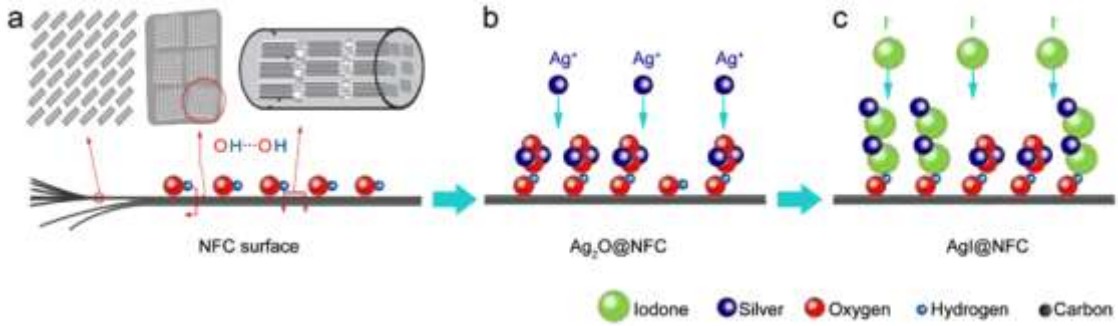

Figure S13. Schematic illustration of the Ag_2O nanocrystal formation on the $(10\ \bar{1})$ plane of cellulose nanofibers (each grey box represents a cellulose chain looking down the chain-axis) within the NFC aerogel and the subsequent deposition of I^- ions (derived from the XRD patterns and FTIR spectra). (a) Surface, cross section, and lateral section of the NFC. (b), (c) The deposition of Ag_2O nanocrystals and subsequent I^- ion adsorption.

Tables

Table S1. Characteristics of the Ag_2O-based nanocomposites with different precursor concentrations.

Sample	$AgNO_3$ (mol dm^{-3})	$NH_3 \cdot H_2O$ (mol dm^{-3})	$Ag(NH_3)_2^+$ (mol dm^{-3})	[a]D_{TEM} (nm)	Inorganic fraction (wt%)
Ag_2O@NFC-005	0.015	0.015	0.005	10±8	54
Ag_2O@NFC-010	0.03	0.03	0.01	16±12	72
Ag_2O@NFC-050	0.15	0.15	0.05	21±16	92

[a] Particle size as determined from fitting a volume-weighted size distribution with a lognormal distribution function based on TEM micrographs.

Table S2. Frequencies (cm^{-1}) of the main signals of Ag_2O@NFC and the assignments.

Absorption band (cm^{-1})	Assignment
3397	O—H stretch (hydrogen-bonded) from 3468
2975	Bonded O—H stretch
2924	O—H deformation of absorbed H_2O
2854	C—O stretch of absorbed CO_2
1456	O—H stretch
1385	H—O—H bend of absorbed H_2O
1161	C(1)—O—C(4) bridge oxygen stretch (asymmetric, glycosidic linkage)
1060	C(3)—OH stretch
1027	C(6)—OH stretch

Table S3. BET surface area and BJH pore diameter of the aerogel samples.

Sample	BET surface area (m^2/g)	BJH adsorption average pore diameter (nm)
NFC aerogel	284.4	27.2
Ag_2O@NFC-005	256.5	25.2
Ag_2O@NFC-010	195.3	16.2
Ag_2O@NFC-050	153.0	15.1
AgI@NFC-050	124.6	13.7

Movies

Movie S1. The 3D representation of the Ag_2O@NFC-100 obtained by electron tomography.

Movie S2. The Ag_2O@NFC aerogel under compressive strains.

References

(1) Cárdenas, G., Cabrera, G., Taboada, E., Miranda, S. P. Chitin Characterization by SEM, FTIR, XRD, and ^{13}C Cross Polarization/Mass Angle Spinning NMR. *J. Appl.Polym.Sci.* **2004**, *93(4)*, 1876-1885.

(2) Park, S., Baker, J. O., Himmel, M. E., Parilla, P. A., Johnson, D. K. Cellulose Crystallinity Index: Measurement Techniques and Their Impact on Interpreting Cellulase Performance. *Biotechnol. Biofuel.* **2010**, *3(1)*, 1.

(3) Shirley D A. High-resolution X-ray Photoemission Spectrum of the Valence Bands of Gold. *Phys. Rev. B* **1972**, *5(12)*, 4709.

(4) Scofield J H. Hartree-Slater Subshell Photoionization Cross-sections at 1254 and 1487 eV. *J. Electron Spectro.* **1976**, *8(2)*, 129-137.

(5) M. P. Seah, Practical Surface Analysis: Auger and X-ray Photoelectron Spectroscopy. *John Wiley & Sons* **1990**.

(6) Seah M P, Dench W A. Quantitative Electron Spectroscopy of Surfaces: a Standard Data Base for Electron Inelastic Mean Free Paths in Solids. *Surf. interface anal.* **1979**, *1(1)*, 2-11.

(7) Barrett E P, Joyner L G, Halenda P P. The Determination of Pore Volume and Area Distributions in Porous Substances. I. Computations from Nitrogen Isotherms. *J. Am. Chem. Soc.* **1951**, *73(1)*, 373-380.

(8) Passe-Coutrin, N., Altenor, S., Cossement, D., Jean-Marius, C., Gaspard, S. Comparison of parameters calculated from the BET and Freundlich Isotherms Obtained by Nitrogen Adsorption on Activated Carbons: A New Method for Calculating the Specific Surface Area. *Micropor. Mesopor.***2008**, *111(1)*, 517-522.

(9) Lu, Y., Sun, Q., She, X., Xia, Y., Liu, Y., Li, J., Yang, D. Fabrication and Characterisation of α-chitin Nanofibers and Highly Transparent Chitin Films by Pulsed Ultrasonication. *Carbohyd. Polym.* **2013**, *98 (2)*, 1497–1504

(10) Yang, D., Sarina, S., Zhu, H., Liu, H., Zheng, Z., Xie, M., Smith, S.V., Komarneni, S. Capturing Radioactive Cs^+ and I^- from Water with Titanate Nanofibers and Nanotubes, *Angew. Chem. Int. Ed.*, **2011**, *50*, 10594-10598.

(11) Martin J E, Fenner F D. Radioactivity in Municipal Sewage and Sludge. *Public Health Rep.* **1997**, *112(4)*, 308.

(12) Yang, D., Liu, H., Zheng, Z., Sarina, S., Zhu, H. Titanate-based Adsorbents for Radioactive Ions Entrapment from Water. *Nanoscale* **2013**, *5(6)*, 2232-2242.

(13) Kumar, S., Surendar, T., Baruah, A., Shanker, V. Synthesis of a Novel and Stable gC_3N_4–Ag_3PO_4 Hybrid Nanocomposite Photocatalyst and Study of the Photocatalytic Activity Under Visible Light Irradiation. *J. Mater. Chem. A*, **2013**, *1(17)*, 5333-5340.

(14) Faisal, M., Khan, S. B., Rahman, M. M., Jamal, A., Akhtar, K., Abdullah, M. M. Role of ZnO-CeO_2 Nanostructures as a Photo-catalyst and Chemi-sensor. *J.Mater. Sci – Technol* **2011**, *27(7)*, 594-600.

(15) Rahman, M. M., Khan, S. B., Asiri, A. M., Alamry, K. A., Al-Youbi, A. O. Detection of Nebivolol Drug based on As-grown Un-doped Silver Oxide Nanoparticles Prepared by a Wet-chemical Method. *Int J Electrochem S.* **2013**, *8*, 323-335.

(16) Lefevre, G., Walcarius, A., Ehrhardt, J. J., & Bessiere, J. Sorption of Iodide on Cuprite (Cu_2O). *Langmuir* **2000**, *16(10)*, 4519-4527.

(17) Liang, H. W., Cao, X., Zhang, W. J., Lin, H. T., Zhou, F., Chen, L. F., Yu, S. H. Robust and Highly Efficient Free-standing Carbonaceous Nanofiber Membranes for Water Purification. *Advanced Functional Materials* **2011**, *21(20)*, 3851-3858.

(18) Liang, H. W., Guan, Q. F., Chen, L. F., Zhu, Z., Zhang, W. J., Yu, S. H. Macroscopic-Scale Template Synthesis of Robust Carbonaceous Nanofiber Hydrogels and Aerogels and Their Applications. *Angew. Chem. Int. Edit.n* **2012**, *51(21)*, 5101-5105.